

Characterizing the dynamical magnetosphere of the extremely slowly rotating magnetic O9.7 V star HD 54879 using rotational modulation of the H α profile

M. KÜKER,¹ S. P. JÄRVINEN,¹ S. HUBRIG,¹ I. ILYIN,¹ AND M. SCHÖLLER²

¹Leibniz-Institut für Astrophysik Potsdam (AIP), An der Sternwarte 16, 14482 Potsdam, Germany

²European Southern Observatory, Karl-Schwarzschild-Str. 2, 85748 Garching, Germany

ABSTRACT

The magnetic field in the O9.7 V star HD54879 has been monitored for almost a decade. Spectropolarimetric observations reveal a rather strong mean longitudinal magnetic field that varies with a period of about 7.41 yr. Observations in the H α line show a variation with the same period, while the H β line shows only little variation. Assuming the periodic variation to be caused by a slow rotation and a dipolar magnetic field, we find a magnetic field strength of ≥ 2 kG at the magnetic poles. With the relatively low mass loss rate of $10^{-9} M_{\odot} \text{ yr}^{-1}$, this star is a case of extremely strong magnetic confinement. Both theoretical arguments and numerical simulations indicate the presence of an extended disk of increased gas density in the equatorial plane of the magnetic field, where gas from the line-driven stellar wind is trapped. This disk is likely to be the origin of the observed H α emission, which peaks together with the strongest line-of-sight magnetic field. The profile of the H α line is resolved in several components and shows a remarkable variability with the rotation period.

Keywords: stars: individual: HD 54879 – stars: early-type – stars: atmospheres – stars: variables: general – stars: magnetic fields

1. INTRODUCTION

The role of massive stars in the evolution of our Universe is widely recognized: massive stars drive energetic physical processes that affect the structure of entire galaxies and chemically enrich the ISM. Magnetic fields are considered to be key components of massive stars with a far-reaching impact on their evolution and ultimate fate: a magnetic mechanism for the collimated explosion of massive stars, relevant for long-duration gamma-ray bursts, X-ray flashes, and asymmetric core collapse supernovae was proposed by [Uzdensky & MacFadyen \(2006\)](#). Magnetic O-type stars with masses larger than $30 M_{\odot}$ and their WR descendants are potentially the progenitors of magnetars ([Gaensler et al. 2005](#)). Magnetars may be the origin of the powering mechanism in both superluminous supernovae and long-duration gamma-ray bursts (e.g. [Yu et al. 2017](#)). Merging of binary compact remnants produces astrophysical transients detectable by gravitational wave observations (e.g. [Abbott et al. 2021](#)).

However, the origin of the magnetism in massive stars and the role the magnetic field plays in their evolution remain unknown. The currently most popular scenario involves a merging event, or mass transfer, or common envelope evolution (e.g. [Tout et al. 2008](#); [Ferrario et al. 2009](#); [Schneider et al. 2016](#)). Mass transfer or stellar merging rejuvenates the mass gaining star, while the induced differential rotation is

thought to be the key ingredient to generate a magnetic field (e.g. [Wickramasinghe et al. 2014](#)).

Previous spectropolarimetric surveys of massive stars indicated that only one short-period binary system, Plaskett’s star, contains a hot, massive, magnetic companion ([Grunhut et al. 2013](#)). On the other hand, a recent study of a representative sample of binary and multiple systems using the European Southern Observatory (ESO) High Accuracy Radial velocity Planet Searcher polarimeter (HARPSpol; [Snik et al. 2008](#)) and the Canada-France-Hawaii Telescope (CFHT) Echelle Spectropolarimetric Device for the Observation of Stars (ESPaDOnS; [Donati et al. 2006](#)), archival spectropolarimetric observations revealed a sizeable sample of binary and multiple systems with magnetic and potentially magnetic components ([Hubrig et al. 2023](#)).

[Castro et al. \(2015\)](#) were the first to report a longitudinal magnetic field of -600 G for the presumably single O9.7 V star HD 54879. Such a field yields to a lower limit of the dipole strength of about 2 kG. [Hubrig et al. \(2020\)](#) reported a possible increase in radial velocity by about 300 m s^{-1} between 2018 January and 2020 December. However, archival VLTI observations did not find any companion to HD 54879 up to 3.5 mag fainter than the primary star ([Järvinen et al. 2022](#)).

The spectropolarimetric observations of HD 54879 acquired over the last decade show a very slow magnetic

field variability related to the extremely slow rotation of HD 54879, which is also indicated in a dynamical spectrum, displaying variability of the $H\alpha$ line (e.g., Järvinen et al. 2022; Hubrig et al. 2020). Assuming that the magnetic field of HD 54879 has a pure dipolar configuration, Järvinen et al. (2022) fitted a cosine curve to the observed distribution of data points obtained from the high-resolution spectropolarimetric observations and determined a stellar rotation period of 7.2 yr. The authors also reported on the anomalous element distribution in the atmosphere of this star: remarkable differences in the measurements using line masks for the elements O, Si, and He were detected on a few epochs close to the best visibility of the negative magnetic field pole. The field strengths measured from He lines were systematically the lowest whereas those from O lines were always higher than those measured from Si lines. Further, the numerical magnetospheric model presented in this work suggests the existence of an enhanced gas density that fills the volume inside the field lines close to the star.

In the following we present recent spectroscopic and polarimetric observations of $H\alpha$, which together with previous observations now cover a time span of 9.9 yr and thus a full rotation period. Based on numerical simulations of the wind originating in HD 54879 using the Nirvana MHD code we present the distribution of mass density and gas velocity amplitude in its magnetosphere. As the magnetosphere is the source of the $H\alpha$ emission observed in massive stars, we discuss the importance of the study of the rotational variability of this emission line to characterize the dynamical magnetosphere around this extremely slowly rotating magnetic star.

2. OBSERVATIONS AND MEAN LONGITUDINAL MAGNETIC FIELD MEASUREMENTS

The observations of HD 54879 presented in this work were obtained with multiple instruments. The Focal Reducer low dispersion Spectrograph (FORS 2; Appenzeller et al. 1998), the Ultraviolet and Visual Echelle Spectrograph (UVES; Dekker et al. 2000), and HARPSpol (Snik et al. 2008) are instruments offered by the ESO, the first two installed at the Very Large Telescope (VLT) on Cerro Paranal, Chile, and the latter one at ESO’s 3.6 m telescope on La Silla, Chile. In addition, we have used in our analysis observations from the high-resolution Potsdam Echelle Polarimetric and Spectroscopic Instrument (PEPSI; Strassmeier et al. 2015) installed at the 2×8.4 m Large Binocular Telescope (LBT) in Arizona and archival spectropolarimetric observations recorded with the ESPaDOnS installed at the CFHT.

The majority of the observations and the data reduction was described in our previous work on HD 54879 (Hubrig et al. 2020; Järvinen et al. 2022). In the following sections only the previously unpublished observations are discussed.

2.1. FORS 2

Two new spectropolarimetric observations of HD 54879 with FORS 2 were obtained on 2022 December 31 and 2023 October 8 in the framework of the ESO programmes 0110.D-0103(A) and 0112.D-2090(A), respectively. The observational setups were in both cases the same as presented previously by Hubrig et al. (2020). We always use a non-standard readout mode with low gain since it provides a broader dynamic range and leads to a higher signal-to-noise ratio (S/N) in the individual spectra. He-Ne-Ar arc lamp exposures are obtained for wavelength calibration. The data extraction is described by Cikota et al. (2017).

2.2. PEPSI

Circular polarized PEPSI data of HD 54879 were obtained on 2022 January 10. For these observations, a different wavelength region was used in comparison to the observations described in Järvinen et al. (2022). Using crossdispersers III and V, the obtained spectra cover the two wavelength regions 4765–5400 Å and 6271–7419 Å. The crossdisperser V was chosen to record the $H\alpha$ line. The observations and the data reduction followed the descriptions given by Järvinen et al. (2022). Additional observations of integral light spectra of HD 54879 with PEPSI were obtained on 2023 December 3. For these observations we used the crossdispersers II, IV, and V covering the wavelength regions 4238–4768 Å, 5389–6283 Å, and 6271–7419 Å, respectively.

2.3. ESPaDOnS

Publicly available and already reduced ESPaDOnS polarimetric spectrum obtained on 2021 February 24 was downloaded from the CFHT archive.

2.4. UVES

In total three new spectra have been recorded with UVES mounted on UT2 of the VLT. The first two spectra were obtained in the framework of the programme 0108.D-0233(B) carried out in 2021 November 29 and 2022 March 1, and one more spectrum was obtained within the programme 0110.D-0103(B) on 2023 March 31. Similar to the previously analysed UVES spectra in Järvinen et al. (2022), the obtained spectra have a resolving power $R \approx 80,000$ in the blue arm (3756–4982 Å) and $R \approx 110,000$ in the red arm (5690–9459 Å). The data was reduced with the ESO Phase 3 UVES pipeline¹.

2.5. HARPSpol

One new spectropolarimetric observation of HD 54879 was obtained on 2024 January 1. Similar to previous HARPSpol data, the spectra have a resolving power of $R \approx$

¹ <http://www.eso.org/rm/api/v1/public/releaseDescriptions/163>

Table 1. Logbook of the so far unpublished high-resolution observations analysed in this paper. The first column gives the instrument used to obtain the spectrum, the second column the time of the observation as modified Julian date (MJD), and the third column the S/N measured near the $H\alpha$ line. The S/N value marked with an asterisk was determined around 5860 \AA because the $H\alpha$ line was not included in those observations. The final column presents the results of the measurements of the longitudinal magnetic field with the spectropolarimetric instruments.

Instrument	MJD	S/N	$\langle B_z \rangle$ [G]
ESPaDOnS	59269.38	313	-494 ± 25
UVES	59548.34	264	–
UVES	59640.13	247	–
UVES	60035.09	190	–
PEPSI	59589.26	586	-404 ± 50
PEPSI	60281.51	411	–
HARPS	60311.08	129	-361 ± 7

Table 2. Logbook of the new low resolution FORS 2 spectropolarimetric observations of HD 54879. The first column gives the modified Julian dates (MJD) at the middle of the exposure and the second column the S/N of the spectra, measured at 4800 \AA . Longitudinal magnetic field measurements, those for the entire spectrum and those using only the hydrogen lines, are presented in Columns 3 and 4. The last column has the measurements using all lines in the null spectra, which are obtained from pairwise differences from all available Stokes V profiles so that the real polarization signal should cancel out.

MJD	S/N	$\langle B_z \rangle_{\text{all}}$ [G]	$\langle B_z \rangle_{\text{hyd}}$ [G]	$\langle B_z \rangle_N$ [G]
59945.35	1314	-513 ± 125	-889 ± 209	87 ± 119
60226.34	2020	-573 ± 69	-895 ± 142	-32 ± 66

115,000 and cover the wavelength range $3780\text{--}6912 \text{ \AA}$ with a gap at $5259\text{--}5337 \text{ \AA}$.

2.6. Longitudinal magnetic field measurements

All new high-resolution observations obtained with and without a Zeeman analyzer are listed in Table 1. The new measurements obtained with FORS 2 are presented in Table 2.

The low-resolution polarimetric spectra obtained with FORS 2 and the high-resolution spectropolarimetric observations with ESPaDOnS, PEPSI and HARPS were used to determine the mean longitudinal magnetic field $\langle B_z \rangle$. The analysis of the ESPaDOnS, PEPSI, and HARPSpol observations, similarly to the work of Hubrig et al. (2020), is based on the least-squares deconvolution (LSD) technique (for details, see Donati et al. 1997). For the ESPaDOnS observation obtained on 2021 February 24 we measure $\langle B_z \rangle = -494 \pm 25 \text{ G}$

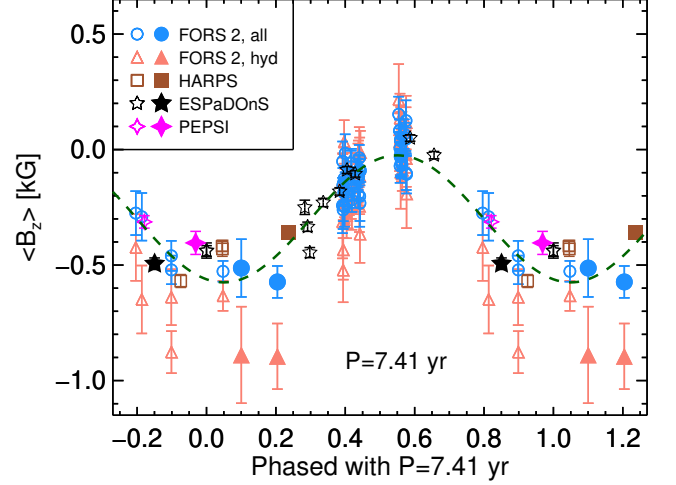


Figure 1. Distribution of the mean longitudinal magnetic field $\langle B_z \rangle$ values of HD 54879 as a function of phase. The smaller open symbols represent data that were published in Järvinen et al. (2022). Larger filled symbols are used to present the new, not previously published, measurements. Circles indicate FORS 2 measurements obtained using the entire spectrum and triangles measurements where only the hydrogen lines were used. Squares, stars, and diamonds indicate measurements using HARPS, ESPaDOnS, and PEPSI high-resolution spectropolarimetric observations, respectively, and are based on a line mask with metal lines. The green dashed line is a sinusoidal fit to the $\langle B_z \rangle$ values with a period of 7.41 yr.

whereas for the PEPSI observation obtained on 2022 January 10 we measure $\langle B_z \rangle = -404 \pm 50 \text{ G}$. The HARPSpol observation obtained on 2024 January 1 gives $\langle B_z \rangle = -361 \pm 7 \text{ G}$. Using the false alarm probabilities (FAPs), following the definitions by Donati et al. (1992), these measurements are definite detections with $\text{FAPs} < 10^{-6}$.

The mean longitudinal magnetic field $\langle B_z \rangle$ using the low-resolution FORS 2 observations obtained on 2022 December 31 and 2023 October 8 were measured following the description given by e.g. Hubrig et al. (2004a,b) and references therein. The error estimations were based on a Monte Carlo bootstrapping test (e.g. Steffen et al. 2014). Similar to our previous studies (Järvinen et al. 2022, and references therein), the FORS 2 field strengths obtained using exclusively hydrogen lines, $\langle B_z \rangle = -889 \pm 209 \text{ G}$ and $\langle B_z \rangle = -895 \pm 142 \text{ G}$, are in absolute value higher than those obtained using the entire spectrum, $\langle B_z \rangle = -513 \pm 125 \text{ G}$ and $\langle B_z \rangle = -573 \pm 69 \text{ G}$.

The new measurements of the mean longitudinal magnetic field values plotted together with older measurements discussed in the past by Järvinen et al. (2022) are presented in Fig. 1 as a function of phase. As magnetic O-type stars are surrounded by magnetospheres, the observed dispersion of data points is usually rather large (e.g. Hubrig et al. 2015; Wade et al. 2015).

As already discussed in Järvinen et al. (2022), the PEPSI spectra cover a much shorter wavelength region than HARPS spectra and even shorter when compared to ESPaDOnS spectra. In comparison to previous PEPSI observations, the covered spectral region in the new PEPSI observation obtained in 2022 (see Section 2.2 for more details) contains only eight useful metal lines. The low number of lines available in the PEPSI spectrum may explain the discrepancy between the latest ESPaDOnS and PEPSI longitudinal magnetic field measurements.

Our observations are in agreement with previous observations of massive O- and B-type stars showing that the magnetic field phase curves usually vary smoothly with a single wave related to a dipolar structure of the magnetic field geometry. Using all available magnetic field measurements covering now 9.9 yr we reformed a period analysis utilizing the Levenberg-Marquardt method (Press et al. 1992), which led to a stellar rotation period of 7.41 ± 0.30 yr.

Only the 54 yr rotation period of the magnetic star HD 108 (Rauw et al. 2023) exceeds that of HD 54879. With the refined period, which within the error is the same as previously reported by Järvinen et al. (2022), the data is fitted with a simple cosine curve illustrated with a dashed dark green line in Fig. 1. From the variation of the longitudinal magnetic field over the rotation period, we determine an average magnetic field of -290 G and a semiamplitude of 275 G.

The effective magnetic field of an oblique dipole rotator is

$$B_e = \frac{1}{20} \frac{15 + u}{3 - u} B_p (\cos \beta \cos i + \sin \beta \sin i \cos \phi) \quad (1)$$

(Stibbs 1950; Preston 1967), where B_p is the polar field strength, u the limb darkening coefficient, i the inclination, β the obliquity, and ϕ the rotational phase. To determine the polar field strength from Equation 1, both the inclination and the obliquity angles would be needed. These angles can not be determined separately from the data. However, from Equation 1 follows

$$r = \frac{B_e^{\min}}{B_e^{\max}} = \frac{\cos(i + \beta)}{\cos(i - \beta)}. \quad (2)$$

We can conclude that $i + \beta \gtrsim 90^\circ$ from the strong asymmetry of the magnetic field variation with respect to zero. From this follows that the dipolar field strength is larger than 1950 G for $i = \beta = 45^\circ$ and reaches values of more than 5 kG for $i = 10^\circ$ or $i = 80^\circ$.

3. H α AND H β VARIABILITY CAUSED BY AN EXTENDED MAGNETOSPHERE

In magnetic massive stars the observed H α line emission is usually dominated by the magnetospheric wind material (e.g., Petit et al. 2013; ud-Doula 2017). As discussed already

in Hubrig et al. (2020), the emission line profiles of H α in HD 54879 are highly variable. Both double- and triple-peak emission profiles were detected. In the observations with the high-resolution instruments used in this study, the H α line is always included, with the exception of PEPSI. The new PEPSI observations include the H α line, but do not cover the H β line, while only the H β line was obtained in observations carried out in 2020.

For massive stars with detected magnetic fields, magnetically trapped wind material frequently leads to rotationally modulated H α emission. In a previous work on HD 54879, Järvinen et al. (2022) reported that the equivalent widths of the H α and H β lines show an increase during the most recent UVES and PEPSI observations, but further monitoring is necessary to confirm this trend. Further, according to Hubrig et al. (2020), the H α lines in the spectra of HD 54879 show variability on time-scales of weeks and even hours. It is possible that this variability is related to the wind or the immediate environment of the star. ud-Doula et al. (2013) suggested that stochastic H α scatter may originate from small differences in the amount of material trapped in the dynamical magnetosphere at any given time.

In Fig. 2 we present all available high-resolution H α profiles overplotted and in Fig. 3 we display them as a dynamical spectrum with time. In Fig. 4 we present the differences of the individual H α profiles with respect to the mean profile as a function of the phase. Both dynamical plots show, when combined with information about the magnetic field strength, that the H α emission is the strongest at the best visibility of the negative magnetic pole.

The behaviour of the hydrogen line H β in HD 54879 has not been studied in similar detail. Albeit the H β profile does not show similar prominent changes as detected in H α , we observe that both the width and depth of this line are variable. A zoom-in to the H β line core is presented in Fig. 5. In order to investigate if there is any correlation between the behaviour of H β and H α profiles, we present the H β profiles as a dynamical spectrum in Fig. 6, which can be compared with Fig. 3. The comparison shows that H β line absorption cores are less deep in the phases when the H α line profile exhibits stronger emission, indicating that the H β lines are most probably filled-in with emission in these phases.

The strong surface magnetic field and the relatively low mass loss rate of HD 54879 lead to an extended magnetosphere, where the gas is trapped by the magnetic field. Shenar et al. (2017) find a value of $10^{-9} M_\odot \text{ yr}^{-1}$ for the mass loss rate if the magnetic field is not taken into account. The impact of the stellar magnetic field on the wind is described by the confinement parameter (ud-Doula & Owocki 2002),

$$\eta_* = \frac{B_{eq}^2 R_*^2}{\dot{M}_{B=0} v_\infty}, \quad (3)$$

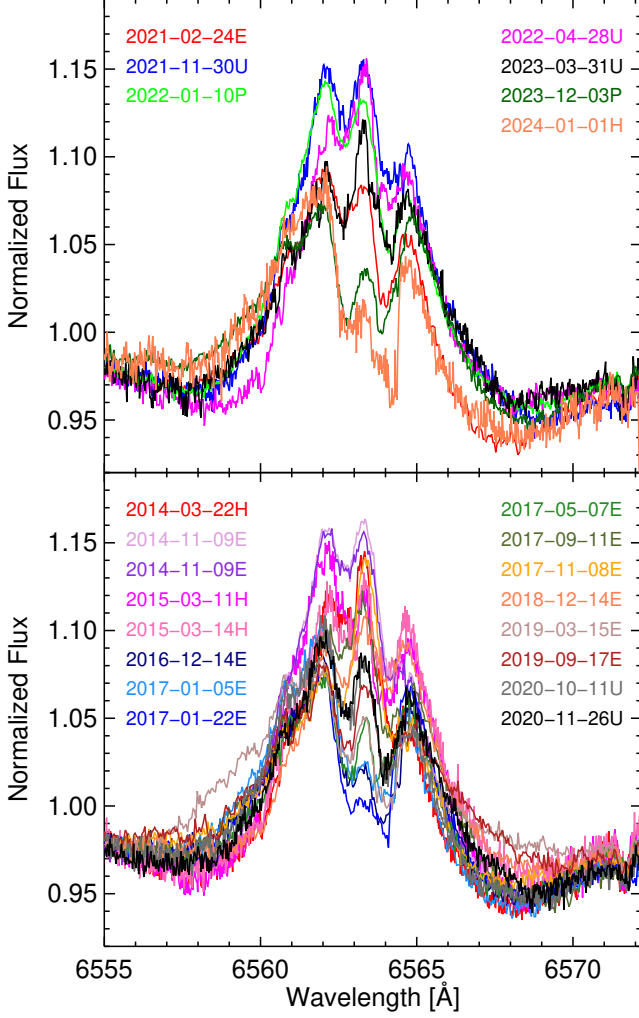


Figure 2. The overplotted $H\alpha$ lines of HD 54879. Each profile is plotted with a different color and the instrument used is indicated after the data: HARPS (H), ESPaDOnS (E), UVES (U), and PEPISI (P). The upper panel shows the profiles based on the new spectra and the bottom panel shows the profiles already published in Järvinen et al. (2022).

where B_{eq} is the magnetic field strength at the equator, R_* the stellar radius; $\dot{M}_{B=0}$ is the mass loss rate and v_∞ the terminal speed found when the magnetic field is ignored. For HD 54879, using a dipolar field with a polar strength of 2 kG and a terminal velocity of 1700 km s^{-1} , this yields a value of 1.7×10^4 and therefore a very extended magnetosphere. For a dipolar field, the Alfvén radius is given by the approximation (ud-Doula et al. 2008)

$$\frac{R_A}{R_*} \approx 0.3 + (\eta_* + 0.25)^{1/4}. \quad (4)$$

From this follows an Alfvén radius of $11.7 R_*$ for $\eta_* = 1.7 \times 10^4$. The farthest closed field line crosses the equator at

$$R_c \approx R_* + 0.7(R_A - R_*). \quad (5)$$

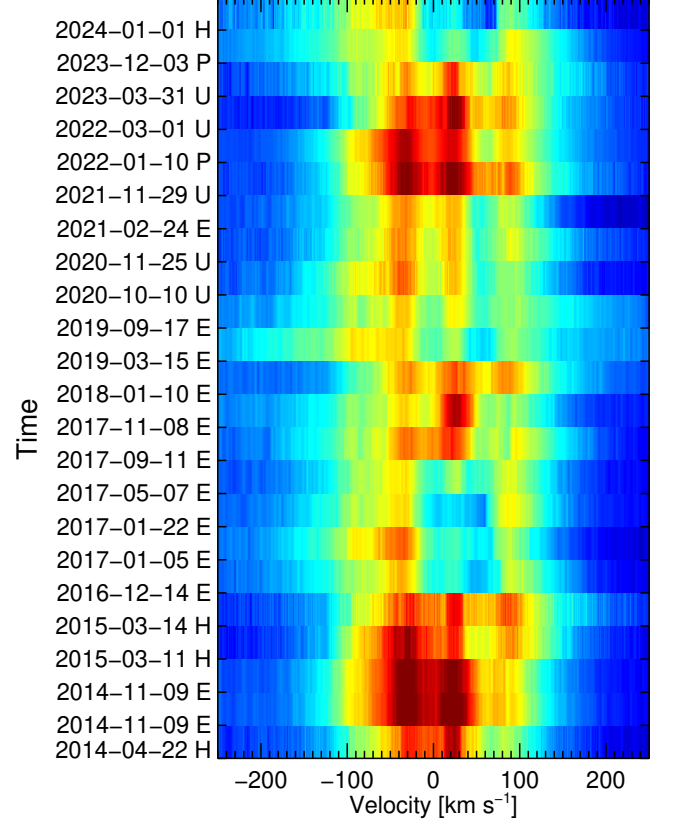


Figure 3. Dynamical spectrum showing the variability of the $H\alpha$ profiles presented in Fig. 2. The red colour corresponds to the strongest emission, while the blue colour shows the $H\alpha$ profile wings appearing in absorption.

With $R_A = 11.7 R_*$, we find $R_c = 8.5 R_*$.

The dynamical impact of the stellar rotation is given by the parameter

$$W = \frac{V_{\text{rot}}}{V_{\text{orb}}} = \frac{\Omega R_*}{\sqrt{GM_*/R_*}}, \quad (6)$$

the ratio of the equatorial rotation speed and the Keplerian orbital speed at the stellar surface. With the rotation period of 7.41 yr derived from the $H\alpha$ variation, a value of 1.8×10^{-4} follows, indicating a negligible impact of the stellar rotation. This is also manifested through the large Kepler corotation radius,

$$R_K = \left(\frac{GM_*}{\Omega^2} \right)^{1/3} = W^{-2/3} R_*, \quad (7)$$

for which we find a value of $313 R_*$. For the rotation to have a significant effect on the structure of the magnetosphere, the Kepler corotation radius must be smaller than the Alfvén radius. In this case, a centrifugal magnetosphere (CM) forms, where the gas corotates with the star. In contrast, in dynamical magnetospheres (DM) the Kepler corotation radius is larger than the Alfvén radius and the gas flows back to the star along the field lines of the magnetic field (Petit et al.

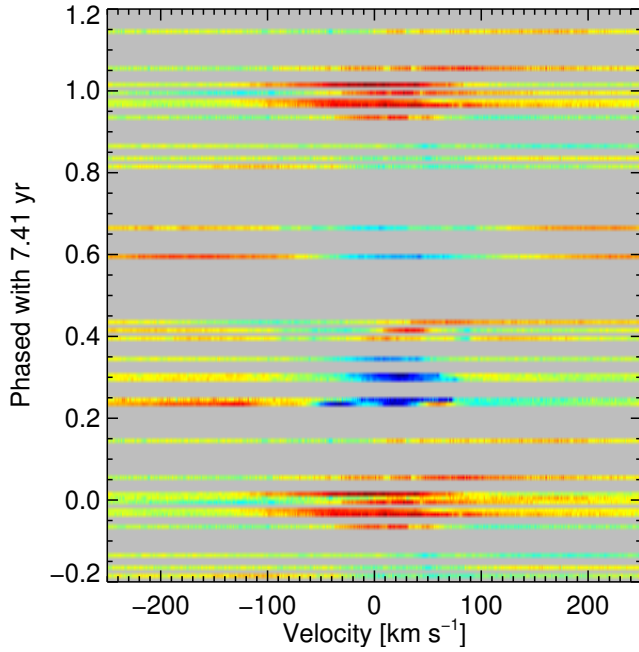


Figure 4. Dynamical spectrum of the differences of the individual $H\alpha$ profiles with respect to the mean profile phased with the period of 7.41 yr.

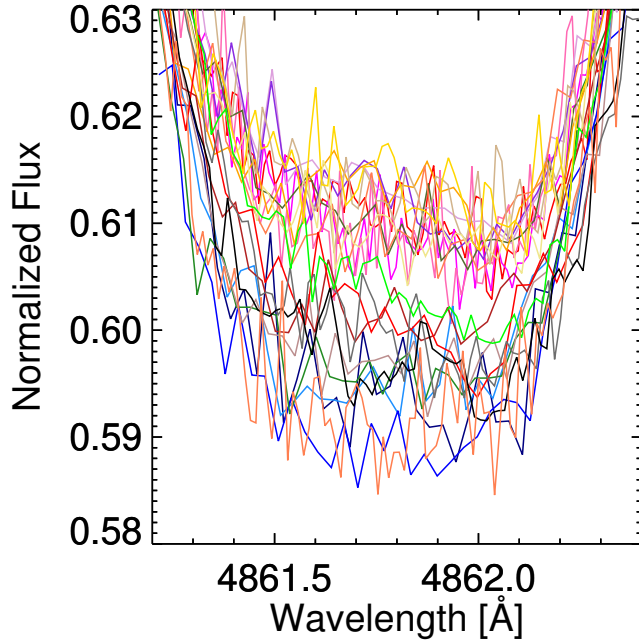


Figure 5. Zoom-in to the core of the $H\beta$ profiles. Each individual spectrum has been plotted with a different color.

2013). In the case of HD 54879 the Kepler corotation radius is much larger than the Alfvén radius and the magnetosphere is thus dynamical.

A comparison of the variations of the magnetic field and the $H\alpha$ emission shows that they both follow the same cy-

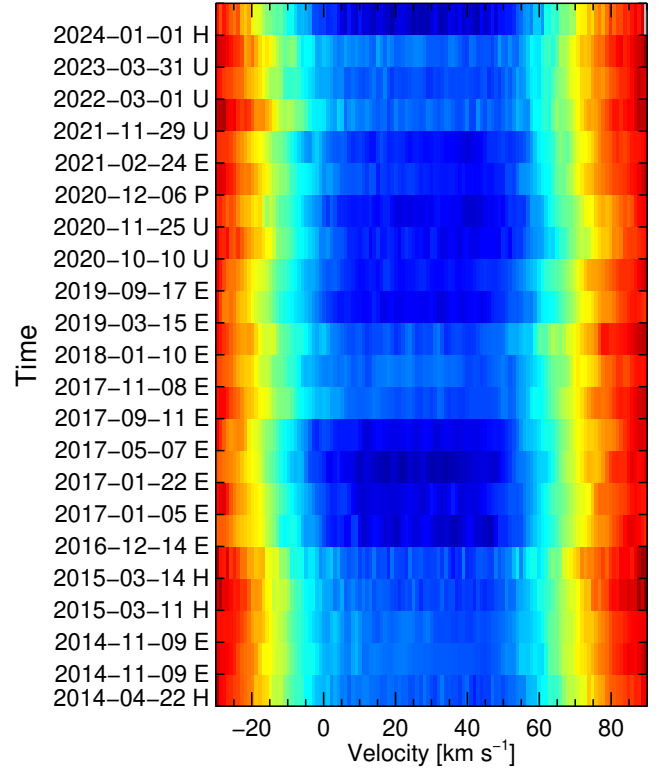


Figure 6. Dynamical presentation of the $H\beta$ core profiles shown in Fig. 5. The darkest blue color shows the deepest absorption whereas the redder the color the closer the profile is to the continuum.

cle, i.e. the stellar rotation. From this we conclude that the star is an oblique rotator with a dipolar magnetic field that is tilted against the rotation axis. As the magnetic field is rather strong, a large fraction of the gas flowing from the star is trapped and forms a magnetosphere centered around the magnetic equator. This magnetosphere is the source of the $H\alpha$ emission and the line width is determined by the velocity of the trapped gas, which is much lower than in the line driven wind along open field lines.

The radial velocity of HD 54879 was first measured by Neubauer (1943), who found a value of $15.6 \pm 1.4 \text{ km s}^{-1}$. More recent measurements found values about twice as high. Boyajian et al. (2007) reports a value of $35.4 \pm 1.4 \text{ km s}^{-1}$ while Castro et al. (2015) found $29.5 \pm 1.0 \text{ km s}^{-1}$ and Hubrig et al. (2020) arrived at $27.0 \pm 0.1 \text{ km s}^{-1}$. Radial velocity of about 30 km s^{-1} follows from dynamical presentation of the $H\beta$ core (Figure 6), inline with the other recent determinations. If we correct for the radial velocity of the star, the side features in Fig. 3 show velocities of about 75 km s^{-1} and -75 km s^{-1} . If these features were caused by an object in keplerian rotation around HD 54879, the orbital radius would have to be 78 stellar radii. An object in corotation with the star, on the other hand, would have to be located at 626 stellar radii to match a velocity of 75 km s^{-1} . Neither assumption seems plausible.

A periodic $H\alpha$ emission pattern has been modelled for a few other magnetic massive stars, θ^1 Ori C, HD 191612, and HD 57682:

θ^1 Ori C rotates with a period of 15.4 d. The mass loss rate is $3.3 \times 10^{-7} M_{\odot} \text{ yr}^{-1}$, and the polar field strength is 1.1 kG (Stahl et al. 2008). The stellar magnetosphere was modelled in both 2D and 3D (Gagné et al. 2005; ud-Doula et al. 2013). The observed variation of the $H\alpha$ line is reproduced in ud-Doula et al. (2013) under the assumption that the magnetic field is tilted by 45° against the rotation axis and that the angle between the rotation axis and the viewing direction of the observer is also 45° . The star and its magnetosphere are then seen pole-on (with respect to the magnetic field) at phase $\phi = 0$ and edge-on at phase $\phi = 0.5$.

HD 191612 is a magnetic O star with a rotation period of 538 d, a mass loss rate of $1.6 \times 10^{-6} M_{\odot} \text{ yr}^{-1}$ and a polar magnetic field strength of 2450 ± 400 G (Howarth et al. 2007; Wade et al. 2011). Sundqvist et al. (2012) modelled the $H\alpha$ emission of HD 191612 based on numerical simulations of the stellar magnetosphere and a line-driven wind. The variation of the longitudinal magnetic field suggests a large obliquity $\beta = 67^\circ$ and an inclination $i = 30^\circ$ while the $H\alpha$ emission was best reproduced with $\beta = i = 50^\circ$.

HD 57682 is an O9 supergiant with a rotation period of 65.4 d and a polar field strength of 880 G (Grunhut et al. 2012). With a mass loss rate of $1.4 \times 10^{-9} M_{\odot} \text{ yr}^{-1}$, a terminal velocity of 1200 km s^{-1} and a radius of $7 R_{\odot}$, the confinement parameter is 1.4×10^4 . Grunhut et al. (2012) were able to model the observed $H\alpha$ variation but had to assume a substantially larger value for the mass loss rate than the value inferred from UV by Grunhut et al. (2009), contrary to the expectation of a mass loss rate lowered by the presence of a magnetic field (ud-Doula et al. 2008). As the magnetic field variation is symmetric with respect to zero, a large obliqueness seems likely for this star.

Figure 7 shows the distributions of mass density and gas velocity amplitude from a numerical simulation using the Nirvana MHD code (Ziegler 2004, 2005) with the setup described in Hubrig et al. (2019). The Nirvana code solves the equation of motion, the induction equation, and the equations of energy and mass conservation for a fully compressible, ionised gas using a finite volume method. We have applied it for an axisymmetric configuration using spherical polar coordinates and an isothermal gas with a dipole field rooted in the star. Both plots display averages over 100 snapshots. The gas flowing from the star is mostly trapped by the magnetic field and accumulates in a disk-shaped region around the equatorial plane. The disk is separated into two regions. Within the Alfvén radius, it is rather thick and the gas moves back to the star in a zig-zag pattern where the motion is almost parallel to the magnetic field. This leads to a comb-like substructure of

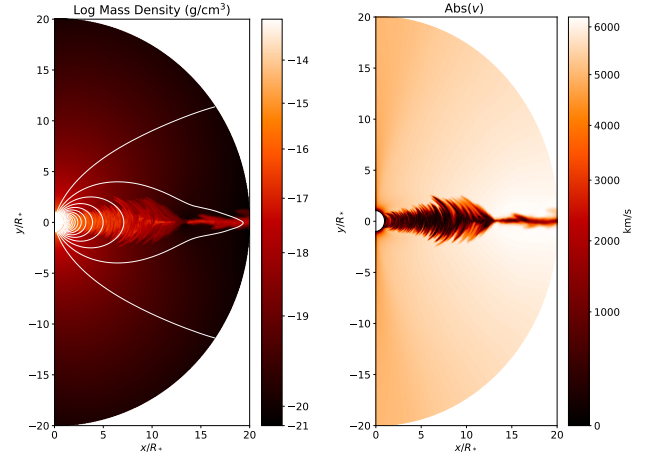


Figure 7. Left: Mass density distribution and magnetic field lines from a numerical simulation of HD 54879. Right: Velocity amplitude.

the inner disk. The outer part of the disk is much thinner and the gas moves outwards, dragging the magnetic field along.

Our model has been tuned to meet the terminal velocity and mass loss rate derived from observations assuming a weak magnetic field. The presence of a strong magnetic field causes a decrease of the mass loss rate and an increase of the terminal velocity. The reduction of the mass loss rate can be explained by the trapping of originally outflowing gas in the region of closed field lines. The increased wind speed was first observed by ud-Doula & Owocki (2002), who attributed it to the divergence of the flow in the open field line region. It is more pronounced in this work as HD 54879 is an extreme case with its high confinement parameter. The discrepancy between the velocity found in the simulations and the observed value of the terminal velocity could be reduced by adjusting the wind force, but that would require a large amount of CPU time and not change the structure of the gas flow in the region of closed field lines.

As the simulation setup is isothermal, we can not model the $H\alpha$ line and have to speculate about the origin of the emission. The Magnetically Controlled Wind Shock (MCWS) model by Babel & Montmerle (1997) predicts the formation of shock fronts in which the outflowing gas is heated up. The heated gas fills the volume between a disk in the equatorial plane and the shock fronts, which are located at mid-latitudes, and is the source of X-ray emission. Babel & Montmerle (1997) originally proposed the MCWS model for the A0p star IQ Aur with a mass loss rate between 10^{-11} to $10^{-10} M_{\odot} / \text{yr}$, a terminal speed $v_{\infty} = 800 \text{ km s}^{-1}$, a polar magnetic field strength $B_0 = 4 \text{ kG}$, and a radius of 5.1 solar radii. From these parameters, a value between 10^6 and 10^7 follows for the confinement parameter, which justifies the assumption of an unperturbed dipole field. As Fig. 7 shows, this is also fulfilled in our simulation up to a certain distance,

after which the magnetic field is stretched away from the star and eventually opens. We can therefore expect the region where an increased density occurs to be the source of X-ray emission. The zig-zag structure is not predicted by the MCWS model, though.

ud-Doula et al. (2014) carried out numerical simulations of the wind confinement of a model star with parameters close to those of the O-type supergiant ζ Pup and confinement parameters of 10 and 100. The simulations included heat transport and cooling and found a shock-heated region at low latitudes outside a radius of about two stellar radii. A zig-zag shaped gas flow back to the star is found in the region of closed field lines near the star, but it changes its direction less frequently than in our simulations. We attribute this difference to the higher value of the confinement parameter and the higher spatial resolution in our simulations.

It should also be noted that as the magnetosphere of HD 54879 is quite extended, its more distant part will never be completely obscured by the stellar disc, though the part closest to the star may be. Moreover, the gas in the equatorial disk outside the radius R_c moves away from the star at speeds much lower than the wind speed above the disk. The left and right features in the dynamical $H\alpha$ spectrum. In the high density region near the magnetic equator, the gas motion is predominantly perpendicular to the equatorial plane. This implies that only a weak Doppler shift would be observed when the disk is seen edge-on.

The $H\alpha$ variation of HD 54879 is in agreement with the picture of an oblique dipole rotator, as derived from the magnetic field variation. The primary maximum at $\phi = 0$ then corresponds to a pole-on view (with respect to the magnetic field and the magnetosphere) while the secondary maximum at $\phi = 0.5$ coincides with the magnetic minimum, i.e. an edge-on view. We can thus rule out extreme values for the inclination angle as neither $i = 0^\circ$, $\beta = 90^\circ$ nor $i = 90^\circ$, $\beta = 0^\circ$ would produce the observed variation. On the other hand, the secondary maximum can not easily be explained as a mere projection effect, as the magnetosphere is presumably seen edge-on. A possible reason could be a significant deviation of either the magnetic field or the magnetosphere from symmetry with respect to the equator or from axisymmetry. We note that in the simulation shown, axisymmetry has been assumed but no symmetry with respect to the equatorial plane has been imposed and the gas distribution does deviate from symmetry on small scales.

4. DISCUSSION

Both theoretical arguments and numerical simulations indicate the presence of an extended disk of increased gas density in the equatorial plane of the magnetic field, where gas from the line-driven stellar wind is trapped. This disk is usually assumed to be the origin of the observed $H\alpha$ emission,

which peaks together with the strongest line-of-sight magnetic field. Already a decade ago, ud-Doula et al. (2013) reported that the magnetically trapped wind material flowing from a star and subsequent gravitational infall of this material yields a circumstellar density high enough to result in strong Balmer line emission. To interpret the $H\alpha$ emission in the magnetic star θ^1 Ori C, the authors analyzed the rotational modulation of this line, using for the first time fully 3D MHD simulations of the magnetic channeling and confinement of its radiatively driven stellar wind. The synthetic $H\alpha$ profiles were computed by solving the formal integral of radiative transfer in a cylindrical coordinate system aligned toward the observer. Although the simulations reproduced quite well both the magnitude and phase of the observed rotational variation, the observed profiles appeared to exhibit an asymmetry about phase 0.5 that was not found in the applied numerical models. ud-Doula et al. (2013) concluded that such asymmetries may have their origin in, e.g., non-dipolar components of the magnetic field.

The rather clear splitting in the structure of the emission $H\alpha$ profile observed at the phase of best visibility of the negative magnetic pole and the absence of a profile asymmetry similar to that detected in θ^1 Ori C make HD 54879 an ideal target for the application of 3D MHD simulations to model its $H\alpha$ line emission. The presented distinct variability of this line with well separated emission peaks permits to follow the contribution of the gas disk accumulated along the magnetic equator and was not observed in any previously studied magnetic massive O-type star. Obviously, 3D modeling of the $H\alpha$ line emission in HD 54879 will significantly improve our understanding of magnetospheres and channeled wind outflows from magnetic massive stars.

ACKNOWLEDGEMENTS

We thank the anonymous referee for their comments.

Based on observations made with ESO Telescopes at the La Silla Paranal Observatory under programme IDs 0102.D-0234(C), 0106.D-0250(A), 0106.D-0250(B), 0108.D-0233(B), 0110.D-0103(A), 0110.D-0103(B), 0112.D-2090(A), and 112.25MG.001.

Based on data acquired with the Potsdam Echelle Polarimetric and Spectroscopic Instrument (PEPSI) using the Large Binocular Telescope (LBT) in Arizona. The LBT is an international collaboration among institutions in the United States, Italy, and Germany. LBT Corporation partners are the University of Arizona on behalf of the Arizona university system; Istituto Nazionale di Astrofisica, Italy; LBT Beteiligungsgesellschaft, Germany, representing the Max-Planck Society, the Leibniz-Institute for Astrophysics Potsdam (AIP), and Heidelberg University; the Ohio State University; and the Research Corporation, on behalf of the University of Notre Dame, University of Minnesota, and Uni-

versity of Virginia. Based on observations collected at the Canada-France-Hawaii Telescope (CFHT), which is operated by the National Research Council of Canada, the Institut National des Sciences de l'Univers of the Centre National de la Recherche Scientifique of France, and the University of Hawaii.

DATA AVAILABILITY

The data obtained with ESO facilities will be available in the ESO Archive at <http://archive.eso.org/> and can be found with the instrument and object name. The ESPaDOnS data underlying this article are available in the CFHT Science Archive at <https://www.cadc-ccda.hia-ihp.nrc-cnrc.gc.ca/en/cfht/> and can be accessed with the instrument and object name. The PEPSI data underlying this article will be shared on a reasonable request to the corresponding author.

REFERENCES

- Abbott, R., Abbott, T. D., Abraham, S., et al. 2021, *ApJL*, 913, L7, doi: [10.3847/2041-8213/abe949](https://doi.org/10.3847/2041-8213/abe949)
- Appenzeller, I., Fricke, K., Fürtig, W., et al. 1998, *The Messenger*, 94, 1
- Babel, J., & Montmerle, T. 1997, *A&A*, 323, 121
- Boyajian, T. S., Gies, D. R., Baines, E. K., et al. 2007, *PASP*, 119, 742, doi: [10.1086/520707](https://doi.org/10.1086/520707)
- Castro, N., Fossati, L., Hubrig, S., et al. 2015, *A&A*, 581, A81, doi: [10.1051/0004-6361/201425354](https://doi.org/10.1051/0004-6361/201425354)
- Cikota, A., Patat, F., Cikota, S., & Faran, T. 2017, *MNRAS*, 464, 4146, doi: [10.1093/mnras/stw2545](https://doi.org/10.1093/mnras/stw2545)
- Dekker, H., D'Odorico, S., Kaufer, A., Delabre, B., & Kotzlowski, H. 2000, in *Society of Photo-Optical Instrumentation Engineers (SPIE) Conference Series*, Vol. 4008, *Optical and IR Telescope Instrumentation and Detectors*, ed. M. Iye & A. F. Moorwood, 534–545, doi: [10.1117/12.395512](https://doi.org/10.1117/12.395512)
- Donati, J. F., Catala, C., Landstreet, J. D., & Petit, P. 2006, in *Astronomical Society of the Pacific Conference Series*, Vol. 358, *Solar Polarization 4*, ed. R. Casini & B. W. Lites, 362
- Donati, J. F., Semel, M., Carter, B. D., Rees, D. E., & Collier Cameron, A. 1997, *MNRAS*, 291, 658, doi: [10.1093/mnras/291.4.658](https://doi.org/10.1093/mnras/291.4.658)
- Donati, J. F., Semel, M., & Rees, D. E. 1992, *A&A*, 265, 669
- Ferrario, L., Pringle, J. E., Tout, C. A., & Wickramasinghe, D. T. 2009, *MNRAS*, 400, L71, doi: [10.1111/j.1745-3933.2009.00765.x](https://doi.org/10.1111/j.1745-3933.2009.00765.x)
- Gaensler, B. M., Kouveliotou, C., Gelfand, J. D., et al. 2005, *Nature*, 434, 1104, doi: [10.1038/nature03498](https://doi.org/10.1038/nature03498)
- Gagné, M., Oksala, M. E., Cohen, D. H., et al. 2005, *ApJ*, 628, 986, doi: [10.1086/430873](https://doi.org/10.1086/430873)
- Grunhut, J. H., Wade, G. A., Marcolino, W. L. F., et al. 2009, *MNRAS*, 400, L94, doi: [10.1111/j.1745-3933.2009.00771.x](https://doi.org/10.1111/j.1745-3933.2009.00771.x)
- Grunhut, J. H., Wade, G. A., Sundqvist, J. O., et al. 2012, *MNRAS*, 426, 2208, doi: [10.1111/j.1365-2966.2012.21799.x](https://doi.org/10.1111/j.1365-2966.2012.21799.x)
- Grunhut, J. H., Wade, G. A., Leutenegger, M., et al. 2013, *MNRAS*, 428, 1686, doi: [10.1093/mnras/sts153](https://doi.org/10.1093/mnras/sts153)
- Howarth, I. D., Walborn, N. R., Lennon, D. J., et al. 2007, *MNRAS*, 381, 433, doi: [10.1111/j.1365-2966.2007.12178.x](https://doi.org/10.1111/j.1365-2966.2007.12178.x)
- Hubrig, S., Järvinen, S. P., Ilyin, I., Schöller, M., & Jayaraman, R. 2023, *MNRAS*, 521, 6228, doi: [10.1093/mnras/stad730](https://doi.org/10.1093/mnras/stad730)
- Hubrig, S., Järvinen, S. P., Schöller, M., & Hummel, C. A. 2020, *MNRAS*, 491, 281, doi: [10.1093/mnras/stz3046](https://doi.org/10.1093/mnras/stz3046)
- Hubrig, S., Küker, M., Järvinen, S. P., et al. 2019, *MNRAS*, 484, 4495, doi: [10.1093/mnras/stz198](https://doi.org/10.1093/mnras/stz198)
- Hubrig, S., Kurtz, D. W., Bagnulo, S., et al. 2004a, *A&A*, 415, 661, doi: [10.1051/0004-6361:20031380](https://doi.org/10.1051/0004-6361:20031380)
- Hubrig, S., Szeifert, T., Schöller, M., Mathys, G., & Kurtz, D. W. 2004b, *A&A*, 415, 685, doi: [10.1051/0004-6361:20031486](https://doi.org/10.1051/0004-6361:20031486)
- Hubrig, S., Schöller, M., Kholtygin, A. F., et al. 2015, *MNRAS*, 447, 1885, doi: [10.1093/mnras/stu2516](https://doi.org/10.1093/mnras/stu2516)
- Järvinen, S. P., Hubrig, S., Schöller, M., et al. 2022, *MNRAS*, 510, 4405, doi: [10.1093/mnras/stab3720](https://doi.org/10.1093/mnras/stab3720)
- Neubauer, F. J. 1943, *ApJ*, 97, 300, doi: [10.1086/144524](https://doi.org/10.1086/144524)
- Petit, V., Owocki, S. P., Wade, G. A., et al. 2013, *MNRAS*, 429, 398, doi: [10.1093/mnras/sts344](https://doi.org/10.1093/mnras/sts344)
- Press, W. H., Teukolsky, S. A., Vetterling, W. T., & Flannery, B. P. 1992, *Numerical recipes in C. The art of scientific computing*
- Preston, G. W. 1967, *ApJ*, 150, 547, doi: [10.1086/149358](https://doi.org/10.1086/149358)
- Rauw, G., Nazé, Y., ud-Doula, A., & Neiner, C. 2023, *MNRAS*, 521, 2874, doi: [10.1093/mnras/stad693](https://doi.org/10.1093/mnras/stad693)
- Schneider, F. R. N., Podsiadlowski, P., Langer, N., Castro, N., & Fossati, L. 2016, *MNRAS*, 457, 2355, doi: [10.1093/mnras/stw148](https://doi.org/10.1093/mnras/stw148)
- Shenar, T., Oskina, L. M., Järvinen, S. P., et al. 2017, *A&A*, 606, A91, doi: [10.1051/0004-6361/201731291](https://doi.org/10.1051/0004-6361/201731291)
- Snik, F., Jeffers, S., Keller, C., et al. 2008, in *Society of Photo-Optical Instrumentation Engineers (SPIE) Conference Series*, Vol. 7014, *Ground-based and Airborne Instrumentation for Astronomy II*, ed. I. S. McLean & M. M. Casali, 701400, doi: [10.1117/12.787393](https://doi.org/10.1117/12.787393)
- Stahl, O., Wade, G., Petit, V., Stober, B., & Schanne, L. 2008, *A&A*, 487, 323, doi: [10.1051/0004-6361:200809935](https://doi.org/10.1051/0004-6361:200809935)
- Steffen, M., Hubrig, S., Todt, H., et al. 2014, *A&A*, 570, A88, doi: [10.1051/0004-6361/201423842](https://doi.org/10.1051/0004-6361/201423842)
- Stibbs, D. W. N. 1950, *MNRAS*, 110, 395, doi: [10.1093/mnras/110.4.395](https://doi.org/10.1093/mnras/110.4.395)

- Strassmeier, K. G., Ilyin, I., Järvinen, A., et al. 2015, *Astronomische Nachrichten*, 336, 324, doi: [10.1002/asna.201512172](https://doi.org/10.1002/asna.201512172)
- Sundqvist, J. O., ud-Doula, A., Owocki, S. P., et al. 2012, *MNRAS*, 423, L21, doi: [10.1111/j.1745-3933.2012.01248.x](https://doi.org/10.1111/j.1745-3933.2012.01248.x)
- Tout, C. A., Wickramasinghe, D. T., Liebert, J., Ferrario, L., & Pringle, J. E. 2008, *MNRAS*, 387, 897, doi: [10.1111/j.1365-2966.2008.13291.x](https://doi.org/10.1111/j.1365-2966.2008.13291.x)
- ud-Doula, A. 2017, *Astronomische Nachrichten*, 338, 944, doi: [10.1002/asna.201713394](https://doi.org/10.1002/asna.201713394)
- ud-Doula, A., Owocki, S., Townsend, R., Petit, V., & Cohen, D. 2014, *MNRAS*, 441, 3600, doi: [10.1093/mnras/stu769](https://doi.org/10.1093/mnras/stu769)
- ud-Doula, A., & Owocki, S. P. 2002, *ApJ*, 576, 413, doi: [10.1086/341543](https://doi.org/10.1086/341543)
- ud-Doula, A., Owocki, S. P., & Townsend, R. H. D. 2008, *MNRAS*, 385, 97, doi: [10.1111/j.1365-2966.2008.12840.x](https://doi.org/10.1111/j.1365-2966.2008.12840.x)
- ud-Doula, A., Sundqvist, J. O., Owocki, S. P., Petit, V., & Townsend, R. H. D. 2013, *MNRAS*, 428, 2723, doi: [10.1093/mnras/sts246](https://doi.org/10.1093/mnras/sts246)
- Uzdensky, D. A., & MacFadyen, A. I. 2006, *ApJ*, 647, 1192, doi: [10.1086/505621](https://doi.org/10.1086/505621)
- Wade, G. A., Howarth, I. D., Townsend, R. H. D., et al. 2011, *MNRAS*, 416, 3160, doi: [10.1111/j.1365-2966.2011.19265.x](https://doi.org/10.1111/j.1365-2966.2011.19265.x)
- Wade, G. A., Barbá, R. H., Grunhut, J., et al. 2015, *MNRAS*, 447, 2551, doi: [10.1093/mnras/stu2548](https://doi.org/10.1093/mnras/stu2548)
- Wickramasinghe, D. T., Tout, C. A., & Ferrario, L. 2014, *MNRAS*, 437, 675, doi: [10.1093/mnras/stt1910](https://doi.org/10.1093/mnras/stt1910)
- Yu, Y.-W., Zhu, J.-P., Li, S.-Z., Lü, H.-J., & Zou, Y.-C. 2017, *ApJ*, 840, 12, doi: [10.3847/1538-4357/aa6c27](https://doi.org/10.3847/1538-4357/aa6c27)
- Ziegler, U. 2004, *Journal of Computational Physics*, 196, 393, doi: [10.1016/j.jcp.2003.11.003](https://doi.org/10.1016/j.jcp.2003.11.003)
- . 2005, *Computer Physics Communications*, 170, 153, doi: [10.1016/j.cpc.2005.04.002](https://doi.org/10.1016/j.cpc.2005.04.002)